

# Bio-Metamaterials for Mechano-Regulation of Mesenchymal Stem Cells

Natalie Munding, Magdalena Fladung, Yi Chen, Marc Hippler, Anthony D. Ho, Martin Wegener,\* Martin Bastmeyer,\* and Motomu Tanaka\*

Cell behaviors significantly depend on the elastic properties of the microenvironments, which are distinct from commonly used polymer-based substrates. Artificial elastic materials called metamaterials offer large freedom to adjust their effective elastic properties as experienced by cells, provided (i) the metamaterial unit cell is sufficiently small compared to the biological cell size and (ii) the metamaterial is sufficiently soft to deform by the active cell contraction. Thus, metamaterials targeting bio-applications (bio-metamaterials) appear as a promising path toward the mechanical control of stem cells. Herein, human mesenchymal stem cells (hMSCs) are cultured on three different types of planar periodic elastic metamaterials. To fulfill the above two key requirements, microstructured bio-metamaterials have been designed and manufactured based on a silicon elastomer-like photoresist and two-photon laser printing. In addition to the conventional morphometric and immunocytochemical analysis, the traction force that hMSCs exert on metamaterials are inferred by converting the measured displacement-vector fields into force-vector fields. The differential responses of hMSCs, both on the cellular level and the sub-cellular level, correlate with the calculated effective elastic properties of the bio-metamaterials, suggesting the potential of bio-metamaterials toward mechanical regulation of cell behaviors by the arrangement of unit cells.

## 1. Introduction

Metamaterials are rationally designed artificial solids in that the atoms of ordinary solids are replaced by tailored functional building blocks serving as unit cells that can be arranged into a periodic lattice. This concept allows for obtaining effective metamaterial behavior that goes beyond that of the ingredient materials and that can be highly unusual or even unprecedented. Thereby, metamaterials have enabled novel behavior and potential applications in mechanics,<sup>[1]</sup> electromagnetism/optics,<sup>[2]</sup> and transport.<sup>[3]</sup>

Here, we investigate the possibility of applying metamaterials as bio-materials, called “bio-metamaterials” in the following. The targeted application is to mechanically control the behavior of living cells adhering to the bio-metamaterial via its tailored effective elastic properties. It has been unclear and has been debated whether the effective metamaterial properties have any relevance at all for the behavior of living cells. Moreover, the meaning of effective

N. Munding, M. Tanaka  
Physical Chemistry of Biosystems  
Institute of Physical Chemistry  
Heidelberg University  
69120 Heidelberg, Germany  
E-mail: tanaka@uni-heidelberg.de  
M. Fladung, M. Bastmeyer  
Cell and Neurobiology  
Zoological Institute  
Karlsruhe Institute of Technology (KIT)  
76131 Karlsruhe, Germany  
E-mail: martin.bastmeyer@kit.edu

Y. Chen, M. Hippler, M. Wegener  
Institute of Nanotechnology and Institute of Applied Physics  
Karlsruhe Institute of Technology (KIT)  
76128 Karlsruhe, Germany  
E-mail: martin.wegener@kit.edu

A. D. Ho  
Department of Medicine V  
Heidelberg University  
69120 Heidelberg, Germany

A. D. Ho, M. Bastmeyer, M. Tanaka  
Center for Integrative Medicine and Physics  
Institute for Advanced Study  
Kyoto University  
Kyoto 606-8501, Japan

M. Bastmeyer  
Institute for Biological and Chemical Systems – Biological Information  
Processing (IBCS-BIP)  
Karlsruhe Institute of Technology (KIT)  
76344 Eggenstein-Leopoldshafen, Germany

 The ORCID identification number(s) for the author(s) of this article can be found under <https://doi.org/10.1002/adfm.202301133>

© 2023 The Authors. Advanced Functional Materials published by Wiley-VCH GmbH. This is an open access article under the terms of the Creative Commons Attribution-NonCommercial License, which permits use, distribution and reproduction in any medium, provided the original work is properly cited and is not used for commercial purposes.

DOI: 10.1002/adfm.202301133

metamaterial properties has been discussed more broadly, even outside of biology and outside of mechanics.<sup>[4]</sup> For wave problems, it is often argued that a description in terms of effective metamaterial parameters is justified if and only if the wavelength is much larger than the size of one metamaterial unit cell. This reasoning does not work for the static or quasi-static case of interest here because the wavelength is formally infinite. Therefore, the question is what the living cell really “feels”. Does it experience only the local contacts to the metamaterial structure? If yes, the cell’s response would be solely determined by the properties of the material the metamaterial is made of. In this case, different metamaterials made from the same constituent material would lead to the same response of the living cell. In the opposite limit, the period of the metamaterial is much smaller than the size of the living cell such that one expects that the cell “sees” the effective metamaterial properties by averaging over the underlying microstructure. However, it is unclear what “much smaller” means in practice. In reality, the state-of-the-art manufacturing does not yet allow the realization of metamaterial periods that are hundred or thousand times smaller than the extent of the considered living cell (typically some tens of micrometer). So far, the literature has not yet provided an answer to this crucial question. We will see below that metamaterial periods that are merely 3–8 times smaller than the size of the living cell are already sufficient.

If the effective metamaterial properties do determine the cell behavior, the effective elastic properties can be parameterized and quantified by the effective Young’s modulus, the effective Poisson’s ratio and the effective shear moduli. It is well established that biological cells are controlled by the extrinsic biochemical cues like chemokines and growth factors, but they also probe the mechanical properties from their microenvironment, such as the topography and stiffness of extracellular matrix (ECM).<sup>[5]</sup> To date, a number of studies have shown the critical roles of bulk Young’s modulus of polymer-based substrates in directing the fate of stem cells.<sup>[6]</sup> Yet, the control of cell behaviors using metamaterials still remains a challenge in materials science, mainly due to two major requirements. First, as discussed above, the size of a metamaterial’s unit cell must be sufficiently small compared to the biological cell under consideration. Second, the metamaterial should be deformable by the traction force generated by biological cells, typically on the order of nN to tens of nN, so that the strain-sensitive mechano-sensing machineries, called “molecular clutches”, can respond to the material’s elasticity.<sup>[7]</sup> Corresponding materials (photoresists) for 3D laser printing that allow for achieving sufficiently soft mechanical behavior of the constituent material, and, at the same time, the sufficiently small features necessary for small metamaterial periods have only become available quite recently.

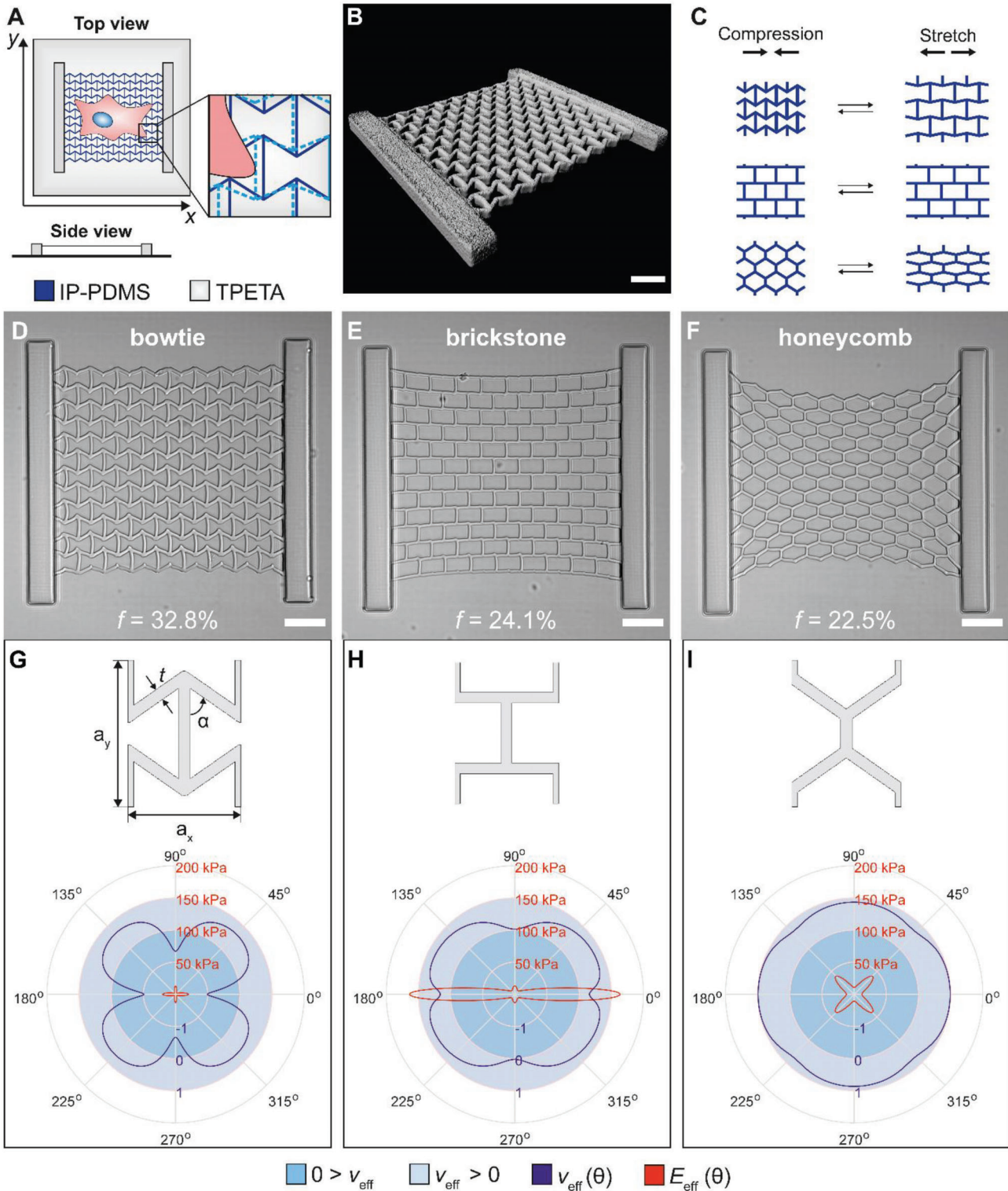
Early steps in this general direction have recently been taken by using three-dimensional, reinforced polyurethane foams or two-dimensional photopolymer meshworks printed by laser lithography.<sup>[8]</sup> Although the feasibility of materials for cell culture and potential applications in stem cell differentiation and tissue engineering has been shown,<sup>[8c,e]</sup> a quantitative understanding of the mechanical interactions of biological cells and metamaterials is still missing both on the cellular and sub-cellular level. Herein, we go beyond this previous work and fabricate three types of metamaterials, which we call *bowtie*, *brickstone*,

and *honeycomb* (Figure 1). We use silicon elastomer-based bio-metamaterials, and calculate the force-vector field of cellular contraction on the basis of measured displacements-vector fields. As the target cells, we select human mesenchymal stem cells derived from bone marrow (hMSCs) that sensitively detect the substrate elasticity and adjust their fate.<sup>[6a,9]</sup> Statistically significant differences in hMSCs behaviors between three bio-metamaterials are observed both on the cellular and sub-cellular level, suggesting that bio-metamaterials provide a new path to mechanically control cell behavior.

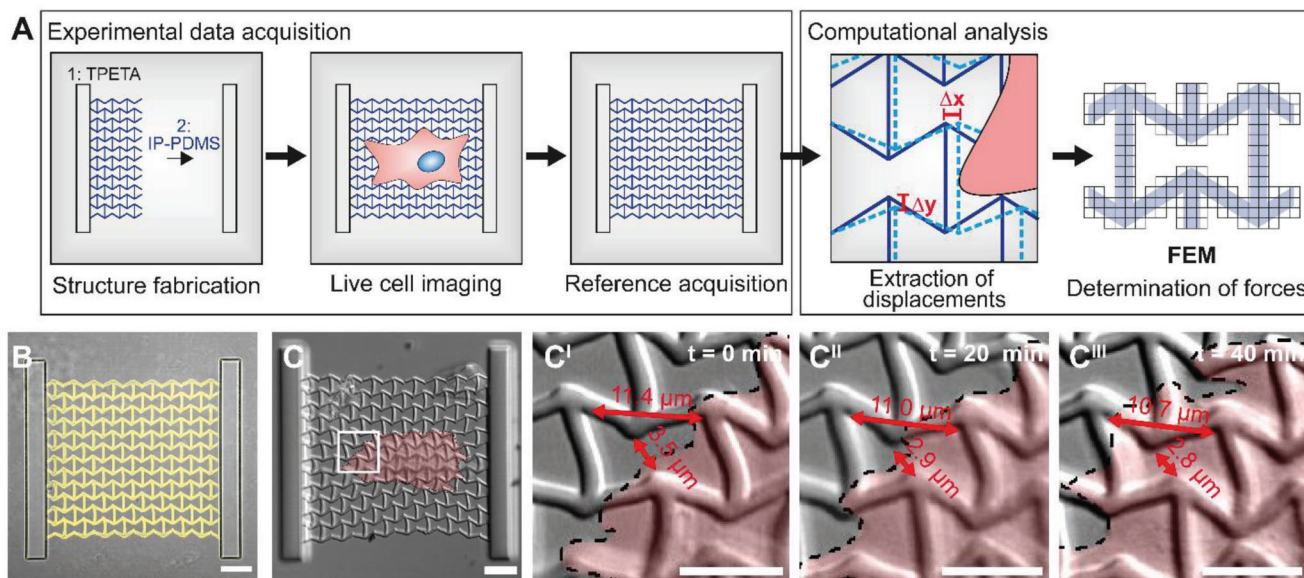
## 2. Results and Discussion

Figure 1 illustrates and defines three different elastic metamaterials that we investigate for their influence on cell behavior in this paper. We select the constituent material to be sufficiently soft such that the cells can induce appreciably large displacements of the structure, allowing them to probe the effective properties of the metamaterial and react correspondingly. We chose the commercial photoresist IP-PDMS (Nanoscribe GmbH & Co. KG, Eggenstein-Leopoldshafen, Germany), which we microstructure by using a commercial 3D laser printer based on two-photon absorption. The printing parameters are given in the Experimental Section. The bulk Young’s modulus of IP-PDMS blocks in water was determined by atomic force microscopy nanoindentation,  $E_{\text{bulk}} = 700$  kPa (Figure S1, Supporting Information). This is more than three orders of magnitude smaller than that of other commonly used photoresists, such as pentaerythritol triacrylate (PETA), whose bulk Young’s modulus in water is  $E_{\text{bulk}} = 3$  GPa.<sup>[10]</sup> In our calculations for IP-PDMS, we assume a bulk Poisson’s ratio of  $\nu_{\text{bulk}} = 0.49$ . We select 2D metamaterial architectures supported by two rigid walls (Figure 1A) that are composed of a different photoresist. In 3D architectures, the refractive-index variations of the transparent metamaterial in water lead to aberrations that hinder high-resolution imaging of the 3D interior. An oblique-view of the laser-printed metamaterial is presented in Figure 1B, showing that the metamaterial net is suspended between two walls and elevated with respect to the substrate surface by 12  $\mu\text{m}$ . This choice allows for detailed high-resolution imaging experiments of the displacement of structures caused by the active contraction of hMSCs seeded on top (Figure 1C). By suspending the metamaterial, we avoid that the cells on the metamaterials have any contact to the glass substrate underneath. Due to printing limitations in regard to large overhanging parts, the distance between the walls is limited. To avoid edge effects due to the mechanically rigid walls, we only consider in our analysis single cells located near the center of the metamaterial.

Out of the infinitely many possibilities of metamaterial structures, we select the three metamaterials shown in Figure 1D–F, which we shall refer to as *bowtie*, *brickstone*, and *honeycomb*, respectively. The unit cells of the three metamaterials are depicted in Figure 1G–I (upper panels). As shown in the polar diagrams, along the direction perpendicular to the walls ( $x$ -axis), *bowtie* has a negative effective Poisson’s ratio ( $\nu_{\text{eff}} < 0$ ), *brickstone* close to zero effective Poisson’s ratio ( $\nu_{\text{eff}} \approx 0$ ), and *honeycomb* a positive effective Poisson’s ratio ( $\nu_{\text{eff}} > 0$ ). The area fractions of the polymer are fairly similar for the three samples:  $f = 32.8\%$  for *bowtie*,  $f = 24.1\%$  for *brickstone*, and  $f = 22.5\%$  for *honeycomb*. This



**Figure 1.** Design of bio-metamaterials used in this study. A) Scheme of the experimental system. 2D metamaterial architectures printed by 3D laser printing based on two-photon absorption. The metamaterial net is supported by two stiff walls and elevated with respect to the glass substrate to avoid direct contact to the glass substrate underneath. Bio-metamaterials made out of soft IP-PDMS can be deformed by cell traction forces. B) Oblique-view of the laser-printed metamaterial obtained by confocal microscopy. Scale bar: 20  $\mu\text{m}$  C) Deformation of three bio-metamaterials under axial stretch and compression. D–F) Differential interference contrast microscopy (DIC) images of three metamaterial nets: *bowtie* D), *brickstone* E), and *honeycomb* F). Scale bars: 20  $\mu\text{m}$ . G–I) Unit cells (upper panels) and calculated bulk effective Young's modulus  $E_{\text{eff}}$  and bulk effective Poisson's ratio  $\nu_{\text{eff}}$  (lower panels) of the three materials in a polar-diagram representation.



**Figure 2.** Flow of live cell imaging and data analysis. A) Flow of data acquisition and image analysis for the force-vector-field calculations. The displacements of the lattice points from the reference were used to calculate a strain-vector map at each time point. See Experimental Section for more details. B) Immunostaining of a *bowtie* metamaterial net made of soft IP-PDMS and functionalized with fibronectin (appearing as yellow). In contrast, the rigid walls on the left and right made out of TPETA are protein repellent. Scale bar: 20  $\mu\text{m}$ . C) DIC image of a human mesenchymal stem cell (hMSC) on a *bowtie* metamaterial net. Scale bar: 20  $\mu\text{m}$ . (C<sup>I</sup>–C<sup>III</sup>) High-magnification images from the region indicated by the white square in C exhibit the change in local displacement vectors, induced by the cellular traction force, at three selected time points. Scale bars: 10  $\mu\text{m}$ .

**Table 1.** Unit cell parameters and effective Young's modulus values of the three metamaterials used in this study.

unit cells	bowtie	brickstone	honeycomb
values			
$a_x$	12.5 $\mu\text{m}$	12.5 $\mu\text{m}$	12.5 $\mu\text{m}$
$a_y$	16.2 $\mu\text{m}$	17.0 $\mu\text{m}$	16.8 $\mu\text{m}$
$\alpha$	55°	90°	125°
$t$	1.3 $\mu\text{m}$	1.3 $\mu\text{m}$	1.3 $\mu\text{m}$
$E_{\text{eff}}(x)$	20 kPa	160 kPa	12 kPa
$E_{\text{eff}}(y)$	13 kPa	13 kPa	11 kPa

means that the three samples provide comparable areas for adhesion points of the cells. This aspect is important because it is known that the available area to form adhesion-points also influences cell behavior.<sup>[11]</sup> The bulk effective Young's modulus  $E_{\text{eff}}$  and the bulk effective Poisson's ratio  $\nu_{\text{eff}}$  of the three samples are obtained by standard numerical finite-element calculations (see Experimental Section). They are graphically illustrated by the polar diagrams in Figure 1G–I (lower panels), emphasizing that the elastic properties are highly anisotropic within the  $xy$ -plane of the metamaterial—as generally expected for periodic mechanical metamaterials. The unit cell parameters and the effective Young's moduli values of the three metamaterials are summarized in **Table 1**. Note that we have fabricated metamaterials with the smallest possible unit cells, the lowest possible area fractions and thicknesses compatible with the printing limitations imposed by the soft IP-PDMS photoresist to fulfill two key re-

quirements: i) the sufficiently small metamaterial unit cell compared to the size of biological cells and ii) the sufficiently soft metamaterial that can deform by the active cell contraction.

We stress that the aim of the present study is not to comprehensively investigate any possible elastic property on any cell behavior, such as, e.g., stem cell differentiation and proliferation. We rather aim to show positive *proof-of-principle* and demonstrate that the elastic properties of rationally designed unit cell structures of bio-metamaterials can have a significant influence on single cells growing on top of the metamaterials, providing a motivation and a starting point for the rational design of bio-metamaterials as a new tool to mechanically control the behavior of various cells.

**Figure 2A** shows the flow of experimental data acquisition. After printing a soft metamaterial net (IP-PDMS) between two walls made out of stiff and protein-repellent trimethylolpropane ethoxylate triacrylate (TPETA, Sigma-Aldrich, St. Louis, MO, USA), the metamaterial surface was functionalized with fibronectin by physisorption. Then, hMSCs were seeded on the top ( $t = 0$  h), allowed to establish a stable adhesion contact ( $t = 0$  h – 1.5 h), and subjected to live cell imaging with confocal microscopy to record the displacement of lattice points ( $t = 1.5$  – 10 h, with images taken every 10 min). The reference data, i.e., the positions of lattice points corresponding to an intact net, could be obtained after the detachment of hMSCs by a trypsin treatment. The displacement-vector field was deduced from the displacement of each lattice point in the  $xy$ -plane. Finally, the force-vector field was calculated using a home-written finite-element-model (FEM) platform (see Experimental Section). In **Figure 2B**, a reference image of the *bowtie* structure functionalized with fibronectin (yellow) and the extracted lattice

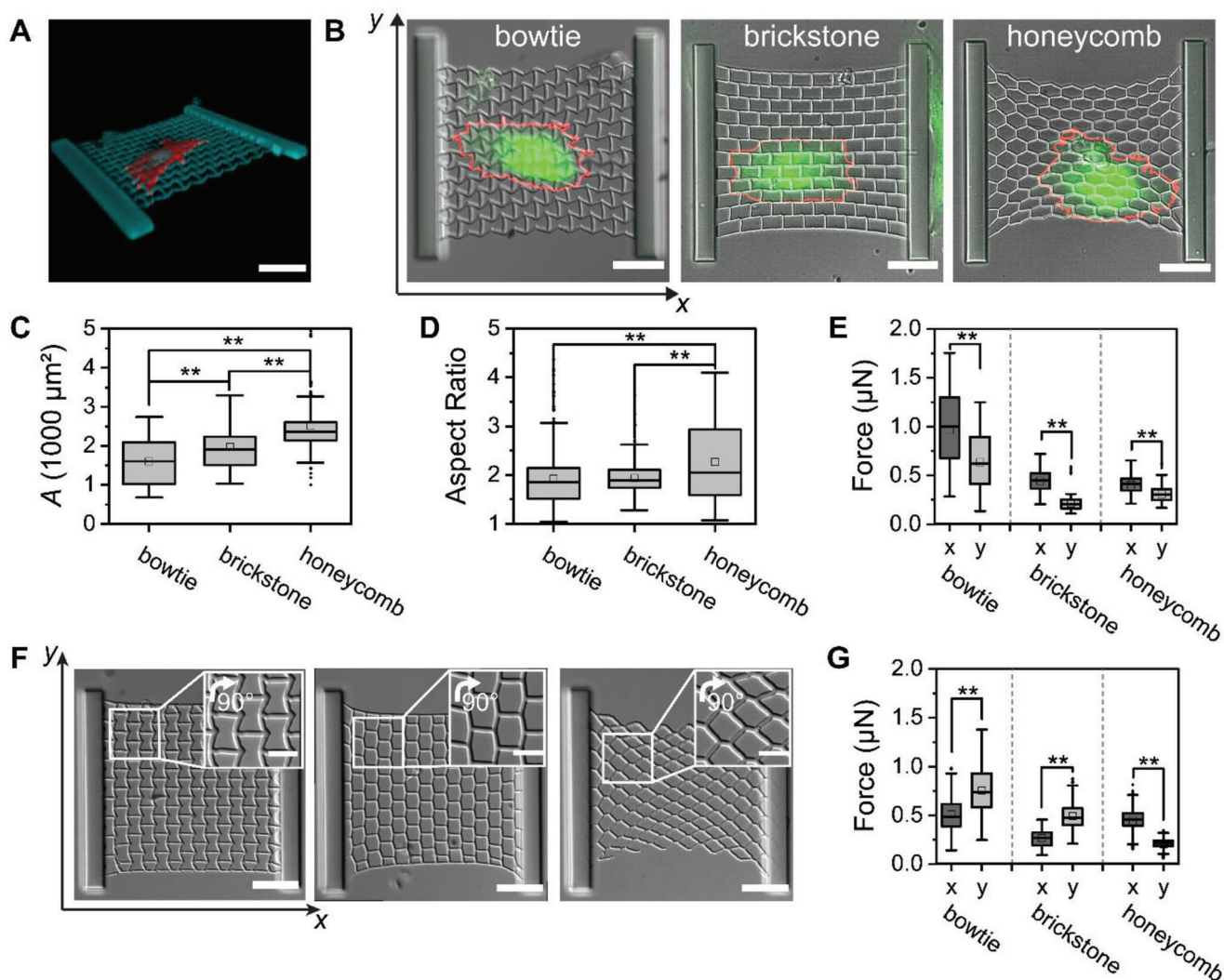


**Figure 3.** Cellular response of hMSCs to bio-metamaterials. A) Oblique image of an hMSC residing on a bio-metamaterial with *bowtie* geometry. Cyan: nucleus, red: actin. Note that the metamaterial net and the rigid walls are visible by their autofluorescence. Scale bar: 30  $\mu\text{m}$ . B) Overlay of cell contours determined by CellBrite Green staining (red lines) and DIC images of the three bio-metamaterials. Scale bars: 30  $\mu\text{m}$ . Panels C) and D) show the comparison of projected area per cell  $A$  and aspect ratio of hMSCs on each metamaterial structure. More than 100 images of  $N \geq 11$  hMSCs were subjected to the analysis of each group. E) Mean traction forces exerted onto the metamaterials, projected in  $x$ - and  $y$ -directions. These forces were calculated from  $>100$  images of  $N \geq 9$  hMSCs. F) Bio-metamaterials with geometry rotated by  $90^\circ$  (scale bars: 30  $\mu\text{m}$ ). High-magnification image of each structure is shown as an inset (scale bars: 10  $\mu\text{m}$ ). G) Mean traction forces on “rotated” metamaterials, deduced from more than 100 images of  $N \geq 7$  hMSCs for each metamaterial structure. The double asterisk indicates a significant difference with  $p$ -value  $< 0.001$  by Student’s  $t$ -test.

structure are presented. Note that rigid TPETA walls are protein repellent and thus not functionalized with fibronectin. Figure 2C shows a snapshot image of an hMSC on a *bowtie* structure, and the high-magnification images from the region indicated by a white box recorded over time are presented in Figure 2C<sup>I</sup>–C<sup>III</sup>, revealing the deformation of the metamaterial unit cells by the traction force exerted by the stem cells.

**Figure 3A** shows an oblique image of a fixed hMSCs on a *bowtie* net collected by confocal microscopy. The actin cytoskeleton is stained with TexasRed-phalloidin (red) and the cell nucleus with DAPI (cyan). The metamaterial and the walls are visible in the DAPI channel due to autofluorescence of IP-PDMS and TPETA. During the live cell imaging (Movies S1–S3, Supporting Information), the contour of hMSC was determined by live cell

staining with CellBrite Green. Figure 3B shows the overlaid DIC and fluorescence images of hMSCs on the three metamaterial structures, highlighting the cell contour from each image in red. Figure 3C,D presents two morphometric cellular parameters: i) the projected area  $A$  and ii) the aspect ratio, extracted from more than 100 images of  $N \geq 11$  hMSCs, respectively. The morphometric parameters were extracted from the timelapse movies (Movies S1–S3, Supporting Information) based on the following two criteria. First, a single cell adheres to a metamaterial net without any contact to the rigid walls or the underlying glass surface. Second, the metamaterial net does not bend or buckle out of the  $xy$ -plane.

The projected area of each hMSC shows a statistically significant difference between the three metamaterials ( $p < 0.001$ ),  $A_{\text{bowtie}} < A_{\text{brickstone}} < A_{\text{honeycomb}}$ . Moreover, the aspect ratio of

hMSCs on *honeycomb* nets is significantly larger than those on *bowtie* and *brickstone* metamaterial nets, suggesting that hMSCs probe and react to the bio-metamaterials with different unit cells. Figure 3E shows the traction forces exerted on the three metamaterials averaged over time projected in  $x$ - and  $y$ -directions, indicating that the strongest forces were exerted on *bowtie* nets. These data could be interpreted partially in terms of the difference in effective Poisson's ratio ( $\nu_{\text{eff}}$ ). The largest  $A$  and aspect ratio obtained on *honeycomb* can be attributed to a positive Poisson's ratio ( $\nu_{\text{eff}} > 0$ , Figure 1I), because the compression of unit cells leads to the expansion in the perpendicular direction, resulting in the elongation of hMSC. In contrast, on *bowtie* with a negative effective positive Poisson's ratio ( $\nu_{\text{eff}} < 0$ ) along both the  $x$ -axis and  $y$ -axis (Figure 1G), the compression of unit cells in  $x$ - or  $y$ -direction results in the compression in the perpendicular direction. On *brickstone* ( $\nu_{\text{eff}} \approx 0$ ), the compression in  $x$ - or  $y$ -direction does not cause the compression or expansion in the other direction.

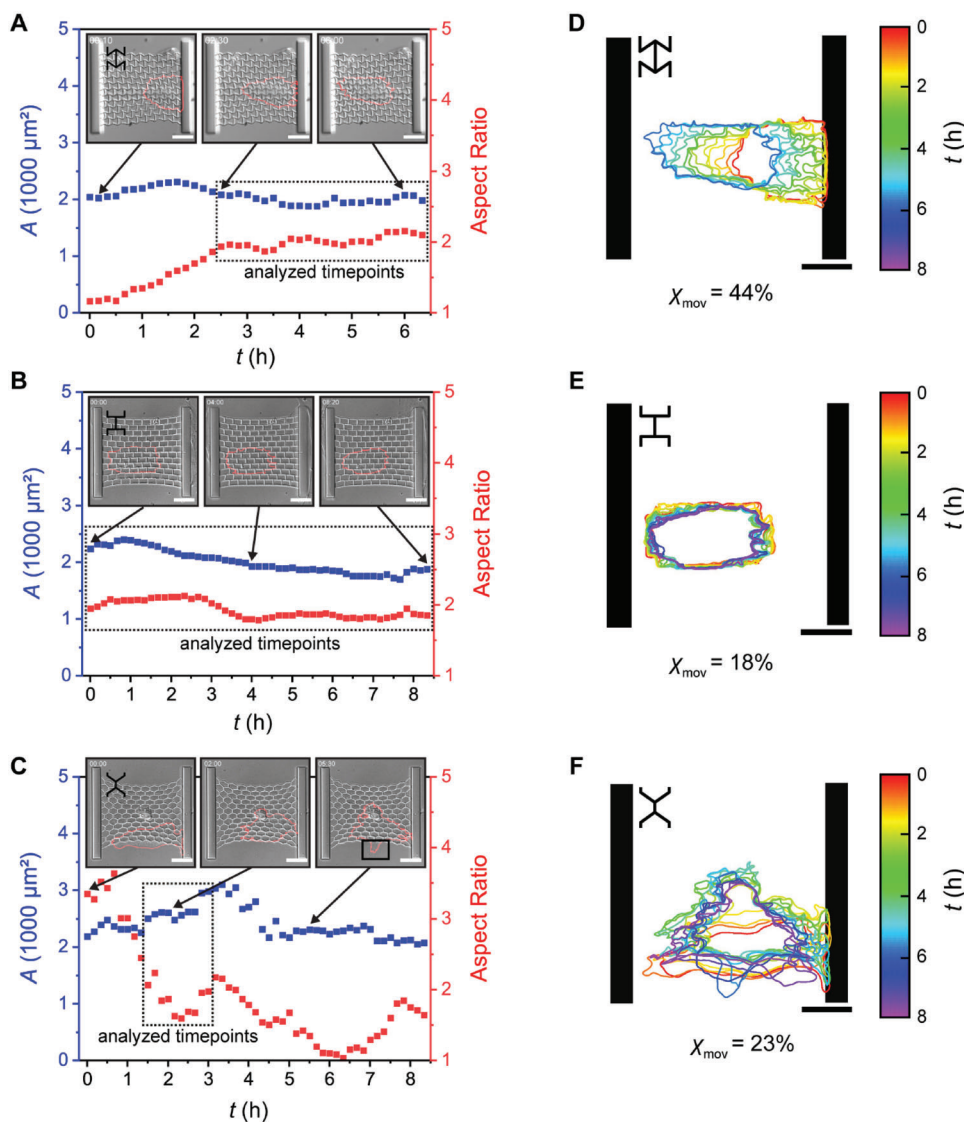
However, the above interpretation ignores two other characteristic properties of our bio-metamaterials, namely the anisotropy of the effective Young's modulus  $E_{\text{eff}}$  (Figure 1G–I) and the edge effect caused by the rigid TPETA walls (Figure 2A). In fact, the mean traction forces in the  $x$ -axis direction are significantly larger compared to those in the  $y$ -axis direction for all three metamaterials (Figure 3E). Note that the  $E_{\text{eff}}$  values of *bowtie* nets in  $x$ - and  $y$ -directions are different,  $E_{\text{eff}}(x) = 20$  kPa and  $E_{\text{eff}}(y) = 13$  kPa. Those of *brickstone* nets showed even a higher anisotropy,  $E_{\text{eff}}(x) = 160$  kPa and  $E_{\text{eff}}(y) = 13$  kPa. On the other hand, the effective Young's modulus  $E_{\text{eff}}$  of the *honeycomb* nets along the two axes are comparable,  $E_{\text{eff}}(x) = 12 \approx E_{\text{eff}}(y) = 11$  kPa. In order to disentangle the two effects, we have printed the metamaterial nets by rotating the geometry by  $90^\circ$  (Figure 3F), while maintaining the orientation of the walls. The calculated mean traction forces exerted on metamaterials are presented in Figure 3G, and the corresponding morphometric parameters, projected area  $A$  and aspect ratio, are presented in Figure S2 (Supporting Information). Notably, the metamaterials with anisotropic effective Young's modulus (*bowtie* and *brickstone*) showed higher forces in  $y$ -direction, which is opposite to the data before rotation (Figure 3E). On the other hand, *honeycomb* nets that have comparable  $E_{\text{eff}}$  values in both directions did not follow this trend. Therefore, we conclude that the anisotropy of  $E_{\text{eff}}$  plays a dominant role in defining the traction force generation compared to the stiff walls.

Figure 4A–C shows the timeseries data as the dynamic changes of the morphometric parameters, projected area  $A$  (blue) and aspect ratio (red), of hMSCs over time, recorded on *bowtie*, *brickstone*, and *honeycomb* metamaterial nets, respectively. The insets show snapshot DIC images of hMSCs corresponding to the time points indicated by black arrows. Dotted boxes mark the time windows that were used to extract the morphometric parameters. The morphometric parameters of cells in contact with the rigid walls are noticeably affected as exemplified for the cells on *bowtie* and *honeycomb* metamaterial nets at  $t = 0$  h (left images, Figure 4A,C). As the morphometric parameters of cells become stable once they lose contact to the walls, only cells located exclusively on the nets were subjected to analysis. During live cell imaging, we noticed that some cells migrated on the bio-metamaterials with an average velocity of  $10\text{--}30 \mu\text{m h}^{-1}$ . Figure 4D–F depicts the outlines of the hMSCs

shown in Figure 4A–C, tracked over 6–8 h, respectively. Notably, the fraction of moving hMSCs is the highest on *bowtie* metamaterial nets ( $\chi_{\text{mov}} = 44\%$ ) as compared to *brickstone* ( $\chi_{\text{mov}} = 18\%$ ) or *honeycomb* ( $\chi_{\text{mov}} = 23\%$ ), which we attribute to the anisotropy of  $E_{\text{eff}}$ .

In the next step, we investigate how hMSCs probe and react to bio-metamaterials on the sub-cellular level. Figure 5A shows the immunocytochemical images of nucleus (blue), vinculin (green), actin (red), and YAP/TAZ (magenta) of hMSCs on bio-metamaterials. hMSCs seeded on fibronectin-coated glass substrates are presented for reference. Vinculin is one of the key adaptor proteins that connect integrin receptors and actomyosin complexes. The traction force generated by the actomyosin complex leads to strain-dependent unfolding of talin, which recruits vinculin to focal adhesions (FAs). This process results in the activation of the transcriptional factor YAP/TAZ thus causing its transport from the cytoplasm to the cell nucleus.<sup>[7b,12]</sup> Figure 5B shows the surface density of FA on the three metamaterials and glass substrates. It is notable that the FA density on the *bowtie* nets is higher than those on *brickstone* and *honeycomb* nets ( $p < 0.05$ ), and is almost comparable to that on glass substrates. As shown in Figure 5C, the nematic order parameter of actin filaments with respect to the major axis of each cell (indicated by a white arrow in Figure 5A) takes the lowest value on *bowtie*, suggesting that the FA-associated actin filaments do not form aligned bundles. A poor order parameter  $\langle S \rangle$  on the *bowtie* metamaterials seems reasonable, because the actin filaments are bound to many FAs confined in small cell-substrate contacts. On the other hand,  $\langle S \rangle$  on the *honeycomb* metamaterial nets is comparable to that on glass substrates, despite of a much lower FA density (Figure 5B). For comparison, the order parameters of actin filaments with respect to the  $x$ -axis are presented in Figure S3 (Supporting Information), showing no significant difference between the three metamaterials. Remarkably, a prominent nuclear localization of YAP/TAZ was observed on the *bowtie* nets, which is clearly different from *brickstone* and *honeycomb*. The nuclear-to-cytoplasmic ratios of YAP/TAZ signals ( $Nuc/Cyto$ ) on the *bowtie* nets are comparable to that on glass substrates (Figure 5D,  $p = 0.25$ ), verifying that the nuclear transfer of YAP/TAZ is tightly coupled to the traction force generated by actomyosin complexes (Figure 3E) and the strain-dependent recruitment of vinculin to FAs (Figure 5B). In fact, the inhibition of myosin II by blebbistatin turned off the nuclear localization of YAP/TAZ on all metamaterials and glass (Figure S4, Supporting Information).

To verify that the mechanical deformation (i.e., strain) of the metamaterial nets is crucial to affect the cell behavior, we performed the same series of experiments on the three metamaterial structures made out of the stiff PETA resist (Sigma-Aldrich, St. Louis, MO, USA) with  $E_{\text{bulk}} = 3$  GPa, rather than the soft IP-PDMS. The morphometric analysis and the immunocytochemical images of vinculin and actin are presented in Figures S5 and S6 (Supporting Information), respectively. Figure 5E,F shows the immunofluorescence images of YAP/TAZ and the  $Nuc/Cyto$  ratio on *bowtie*, *brickstone*, and *honeycomb* nets. For comparison the same control on glass slides is also presented. The morphometric parameters, FA density, actin order parameter  $\langle S \rangle$  and  $Nuc/Cyto$  ratio all showed no difference between the three metamaterials, confirming that the strains caused by



**Figure 4.** Dynamic response of hMSCs to bio-metamaterials. A–C) Time evolution of projected area  $A$  (blue) and aspect ratio (red) of hMSCs on *bowtie*, *brickstone*, and *honeycomb* metamaterial nets extracted from the DIC snapshots of the timelapse movies (Movies S1–S3, Supporting Information), respectively. The time windows used for the morphometric analysis (dotted boxes in A–C) were selected by the two criteria: i) a single cell adheres on a metamaterial net without any contact to the rigid walls or the underlying glass surface, ii) the metamaterial net does not bend or buckle out of the  $xy$ -plane. D–F) Outlines of the same hMSCs presented in Figure A–C tracked over 6–8 h. The fraction of moving cells is given by  $\chi_{\text{mov}}$ . Scale bars:  $30 \mu\text{m}$ .

traction forces are crucial for the mechano-regulation of cells by bio-metamaterials. Note that the IP-PDMS used in this study is currently the softest photoresist ( $E_{\text{bulk}} = 700 \text{ kPa}$ ) available. While hydrogels are softer, stable metamaterial scaffolds with the dimensions used in this work cannot be manufactured with them.

### 3. Conclusion

Previously, little was known about how the anisotropic elasticity, the effective Poisson's ratio and the effective Young's modulus of the surrounding microenvironment affect the functions and fate of stem cells. This shortage was mainly due to the lack of well-defined models of cellular microenvironments. Here, we

designed a new class of bio-metamaterials as a well-defined model for the mechanical control of cells. Free-standing nets of the metamaterials based on a soft, silicon elastomer-like photoresist, microstructured by two-photon laser printing, are supported by two rigid walls and thus decoupled from the underlying substrates. A two-photon laser-printing technique enabled us to manufacture metamaterial unit cells, the size of which is sufficiently small compared to the stem cells. In addition, the soft resistance makes the structure sufficiently compliant to exhibit deformations induced by the active contraction of the stem cells. To compare differential cell behaviors, we fabricated three types of metamaterial structures, *bowtie*, *brickstone*, and *honeycomb*, which possess comparable polymer surface area fractions. These metamaterials structures possess anisotropic elastic properties.

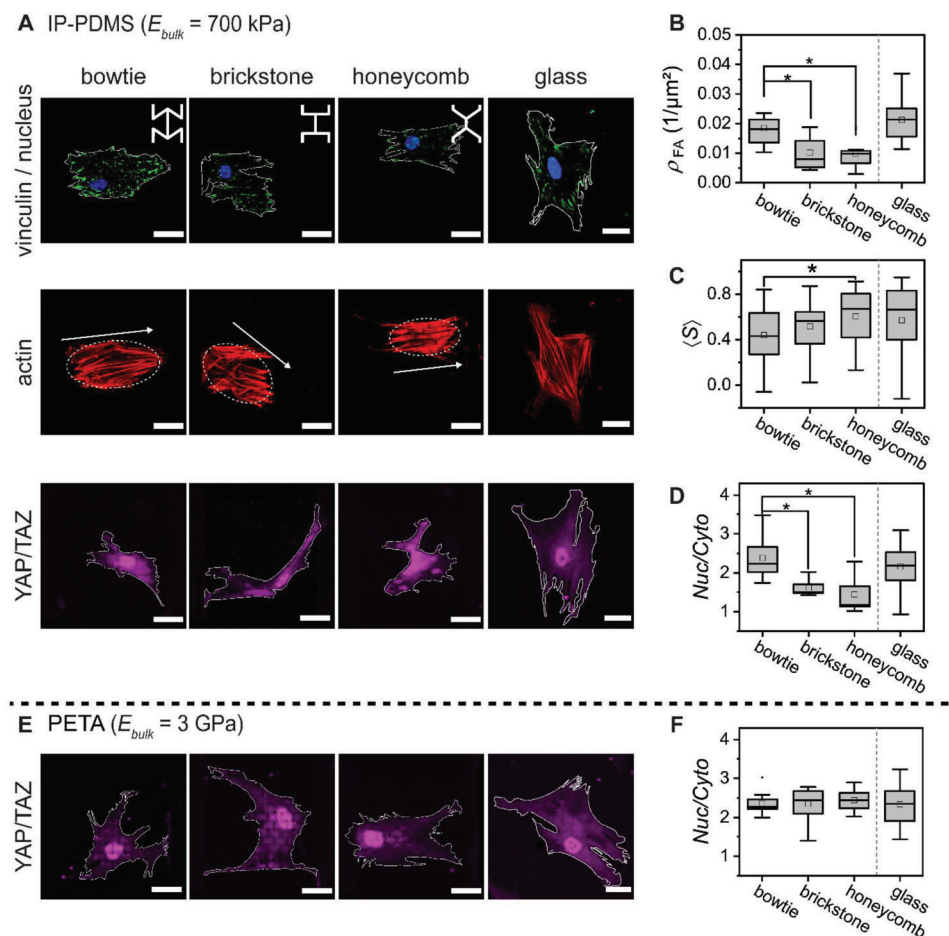


**Figure 5.** Sub-cellular response of hMSCs to bio-metamaterials. A) Immunocytochemical images of hMSCs on bio-metamaterials. Vinculin (focal adhesion); green, DAPI (nucleus); cyan, actin (cytoskeleton); red, and YAP/TAZ (transcriptional factor); magenta. As the reference, the images taken on fibronectin-coated glass substrates are also presented. The contour of each cell is indicated by a white line to guide the eye. Scale bars: 30  $\mu\text{m}$ . B) Surface density of focal adhesion  $\rho_{FA}$  ( $N \geq 11$ ), C) nematic order parameters of filamentous actin  $\langle S \rangle$  ( $N \geq 18$ ), and D) nuclear-to-cytoplasmic ratios of YAP/TAZ signals ( $Nuc/Cyto$ ,  $N \geq 6$ ), respectively. See Experimental Section for the details of analysis. For comparison, YAP/TAZ images and  $Nuc/Cyto$  ratios taken on the stiff PETA ( $E_{bulk} = 3 \text{ GPa}$ ) with the same unit cell geometry are presented in panels E) and F), respectively ( $N \geq 8$ ). Scale bars: 30  $\mu\text{m}$ . The asterisk indicates a significant difference with  $p$ -value  $< 0.05$  by Student's  $t$ -test.

Especially, the effective Poisson's ratios  $\nu_{eff}$  values along the  $x$ -axis assumes different signs, *bowtie* ( $\nu_{eff} < 0$ ), *brickstone* ( $\nu_{eff} \approx 0$ ), and *honeycomb* ( $\nu_{eff} > 0$ ). To enable cell adhesion, the surface of the metamaterial nets was functionalized by the physisorption of fibronectin. In this study, we investigated the behaviors of bone marrow-derived, human mesenchymal stem cells (hMSCs), which are larger than the metamaterial unit cells and for which it is known that their fate is determined by the (effective) bulk Young's modulus of 2D substrates underneath the cells.

First, we investigated the differential behaviors of hMSCs on bio-metamaterials on the cellular level. The morphometric parameters, such as the projected area per cell  $A$  and the aspect ratio, showed clear differences between the three metamaterial structures, which can be interpreted partially in terms of the difference in effective Poisson's ratio ( $\nu_{eff}$ ). To disentangle the anisotropy of the effective Young's modulus  $E_{eff}$  and the edge effect caused by the rigid TPETA walls, we printed the same structures with a  $90^\circ$  rotated geometry and found

that the traction force in  $x$ - and  $y$ -directions on metamaterials with anisotropic Young's modulus showed an inversion. The behavior of hMSCs on the sub-cellular level was further investigated by immunocytochemical staining of focal adhesions (vinculin) and actin (cytoskeletons). Cells probe and interact with the surrounding environment using strain-dependent recruitment of vinculin, resulting in the transfer of transcriptional factor YAP/TAZ to the cell nucleus. The involvement of strain-dependent protein complexes was verified by the behaviors of hMSCs seeded on the same structures made out of stiff PETA ( $E_{bulk} = 3 \text{ GPa}$ ).

This overall demonstrates by positive *proof-of-principle* that the elastic properties of bio-metamaterial can have a significant influence on cells cultured on suitable metamaterials as substrates. This *proof-of-principle* thereby provides motivation and a starting point for the rational design of future bio-metamaterials as a tool to understand and potentially mechanically control the behavior of stem cells and other cell types.

## 4. Experimental Section

**Chemicals:** Polydimethylsiloxane (PDMS, Sylgard 184) was purchased from Dow Corning (Midland, MI, USA), and Mesenchymal Stem Cell growth medium MSCGM was from Lonza (Basel, Switzerland). Texas Red-X phalloidin, vinculin monoclonal antibody (7F9), Alexa Fluor 488 and Goat anti-Mouse IgG (H+L) Highly Cross-Adsorbed Secondary Antibody, Alexa Fluor 647 were obtained from Thermo Fisher Scientific (Waltham, MA, USA). Anti-YAP antibody was purchased from Santa Cruz Biotechnology (Dallas, TX, USA). Rabbit anti-fibronectin antibody was purchased from Sigma-Aldrich (St. Louis, MO, USA). Anti-rabbit IgG Cy5™ was acquired from Jackson ImmunoResearch Europe Ltd. (Cambridge, UK). CellBrite green was purchased from Biotium (Fremont, CA, USA). Bovine serum albumin (BSA), Triton X-100 and toluene were purchased from Carl Roth (Karlsruhe, Germany). (-)-Blebbistatin (blebbi) and fibronectin were purchased from Sigma-Aldrich (St. Louis, MO, USA). IP-PDMS was obtained from Nanoscribe GmbH & Co. KG (Eggenstein-Leopoldshafen, Germany). 3-(trimethoxysilyl)propyl methacrylate, trimethylolpropane ethoxylate triacrylate (TPETA) and pentaerythritol triacrylate (PETA) were obtained from Sigma-Aldrich (St. Louis, MO, USA). Irgacure 819 was acquired from Ciba AG (Basel, Switzerland). Unless stated otherwise, other chemicals were purchased from Sigma-Aldrich (St. Louis, MO, USA) and used without further purification.

**Substrate Functionalization:** To enhance adhesion of the printed microscaffolds to the glass surface, 22 mm × 22 mm high precision cover slips (Paul Marienfeld GmbH & Co. KG (Lauda-Königshofen, Germany)) were cleaned with propan-2-ol and plasma-treated for 10 min. Subsequently, the cleaned cover slips were immersed in a 1.7 mM solution of 3-(trimethoxysilyl)propyl methacrylate in toluene for 1 h at room temperature.<sup>[10]</sup> The functionalized cover slips were rinsed with water and dried with pressurised N<sub>2</sub>.

**Two-Photon Laser Printing:** 3D structures were fabricated using a Photonic Professional GT (Nanoscribe GmbH & Co. KG, Eggenstein-Leopoldshafen, Germany) with a 63× oil immersion objective (NA = 1.4). Fabrication occurred in two sequential writing steps: rigid walls, passivating plates and alignment markers were written from TPETA with 2% (w/w) Irgacure 819 and developed in a 1:1 mixture of propan-2-ol and acetone. A scan speed of 5000–15 000 μm s<sup>-1</sup> and a power scaling of 100% were used. Nets with metamaterial geometry were written between the walls with IP-PDMS or PETA containing 2% (w/w) Irgacure 819. For either case, a scan speed of 1000 μm s<sup>-1</sup> and a power scaling of 65–70% were used. To place the metamaterial nets between the walls, the writing fields were aligned manually with the help of alignment markers. After the samples were developed in propan-2-ol, they were always kept in solvent to avoid the collapse. Prior to use, the structures were washed with propan-2-ol (3 × 5 min) and immersed in water. Finally, the structures were washed with water (3 × 5 min), and the glass slides were glued to petri dishes. After the sterilization under UV light for 1 h, the surface was functionalized with fibronectin (30 μg mL<sup>-1</sup>, in PBS) for 2 h at room temperature to allow for cell adhesion.

**Cell Culture:** hMSCs were isolated and cultured as described before.<sup>[9,13]</sup> The bone marrow from healthy donors was taken after written consent following the guideline approved by the Ethic

Committee on the Use of Human Subjects at Heidelberg University (S-348/2004). The mononuclear cell fraction was isolated by density gradient centrifugation and seeded in plastic culture flasks at a density of 1 × 10<sup>5</sup> cells cm<sup>-2</sup> in MSCGM medium. hMSCs were cultured in MSCGM and at 37 °C under a humidified atmosphere containing 5% CO<sub>2</sub> and the medium was exchanged every 4 d. After 10–14 d, the cells were expanded by splitting the colonies. Throughout this study, hMSCs from early passages (P3–P7) were used.

**Live Cell Imaging:** For live cell imaging hMSCs were labeled in suspension with the membrane dye CellBrite Green™ (Biotium, Fremont, CA, USA) by incubation of 2 × 10<sup>5</sup> cells in 1 mL Hank's Balanced Salt Solution HBSS (140 mM NaCl, 5 mM KCl, 1 mM CaCl<sub>2</sub>·2H<sub>2</sub>O, 0.4 mM MgSO<sub>4</sub>·7H<sub>2</sub>O, 0.5 mM MgCl<sub>2</sub>·6H<sub>2</sub>O, 0.3 mM Na<sub>2</sub>HPO<sub>4</sub>·2H<sub>2</sub>O, 0.4 mM KH<sub>2</sub>PO<sub>4</sub>, 6 mM (+)D-glucose and 4 mM NaHCO<sub>3</sub>) containing 1 μL CellBrite Green. The cells were incubated for 20 min at 37 °C in the dark in the staining solution and subsequently washed with HBSS (1x) and MSCGM (2x). Cells were seeded at a density of 1100 cell cm<sup>-2</sup> and were allowed to adhere for 1.5 h before live cell imaging was started. Live cell imaging was performed using a Zeiss AxioObserver (Zeiss, Oberkochen, Germany) equipped with a 40× oil immersion objective (NA = 1.4) and an incubation chamber sustaining a humidified atmosphere of 37 °C and 5% CO<sub>2</sub>. The setup included a motorized mechanical stage to sequentially move to all the positions during the time series. Images were taken every 10 min over the time of 6–8 h. At the end of the time series, cells were removed using trypsin and a reference image of the scaffold without adherent cell was taken.

**Immunocytochemistry:** Immunostaining was performed to visualize the fibronectin coating, the cell nuclei, actin filaments, the FA protein vinculin and the transcriptional coactivators YAP/TAZ. For visualization of the selective fibronectin coating, metamaterials were coated with fibronectin as described above. The samples were incubated with anti-fibronectin (1:500) in 1% (w/v) BSA in PBS for 1 h at room temperature in the dark, followed by washing with PBS (3 × 5 min) and incubation with secondary antibody anti-rabbit Cy5™ (1:200) in 1% (w/v) BSA in PBS for 1 h at room temperature in the dark. Images were acquired with an LSM800 confocal microscope (Zeiss, Oberkochen, Germany) equipped with a 40× oil immersion objective (NA = 1.4). To visualize the active, cytoskeleton-bound vinculin, cells were incubated with CSK buffer (0.5% (w/v) Triton X-100, 10 mM PIPES pH 6.8, 50 mM NaCl, 3 mM MgCl<sub>2</sub>, 300 mM sucrose) for 1.5 min at 4 °C,<sup>[14]</sup> followed by an immediate fixation with 4% (w/v) PFA in PBS for 15 min at room temperature. Otherwise, cells were fixed using 4% (w/v) PFA in PBS for 15 min at room temperature. For all immunostaining experiments the cells were fixed 6 h after seeding. After fixation the cells were washed with PBS three times for 5 min and subsequently incubated for 5 min with 0.2% Triton X-100. The cells were blocked with 3% (w/v) BSA in PBS for 30 min at room temperature. Following primary antibodies were used: vinculin monoclonal antibody (7F9) conjugated with Alexa Fluor 488 (1:200), anti-YAP (1:100) and Texas Red phalloidin (1:800). The cells were incubated with the primary antibodies in 3% (w/v) BSA overnight at 4 °C (anti-vinculin and anti-YAP) or for 1 h at room temperature (phalloidin). Samples were again washed with PBS (3 ×) and incubated with the fluorescently coupled secondary antibody (Alexa Fluor

647 Goat anti-mouse) for 1 h at room temperature. Nuclei were stained with DAPI (1:1000) for 10 min in PBS. Stained cells were stored at 4°C in the dark. The inhibitor experiments were performed by incubating hMSCs with 50 μM blebbistatin (myosin II blocker, Sigma-Aldrich (St. Louis, MO, USA)) in MSCGM for 4 h. The inhibitor was added 2 h after seeding hMSCs. Images were acquired with a Nikon C2 Plus confocal microscope or a Nikon A1R confocal microscope (Nikon Europe, Düsseldorf, Germany) equipped with a 40× oil immersion objective (NA = 1.4).

**Analysis of Cellular Response:** The morphometric parameters of hMSCs, such as the projected area per cell  $A$  and the aspect ratio, were analyzed using Fiji software.<sup>[15]</sup> The positions of nodes were defined for all unit cells by hand, and the timelapse images were compared to the reference image by image cross-correlation using a custom MatLab code (MathWorks, Natick, MA, USA). 2D displacement vectors obtained from the maximum image cross correlation were used to track the deformation of unit cells. The offsets originating from the stage drift were corrected using Fiji plugin “Linear Stack Alignment with SIFT”.<sup>[15,16]</sup>

**Finite Element Analysis:** Numerical simulations were performed by using the commercial finite element software COMSOL Multiphysics (Göttingen, Germany). To detect the deformation of metamaterial samples more accurately, fluorescence microscope images of the intact metamaterials acquired after the detachment of cells were used as the reference images. Furthermore, pixelated binary images, with black/white pixels representing solids/voids, were derived from the fluorescence images by setting a manual threshold using Fiji software.<sup>[15]</sup> To reduce computation costs, the pixelated images were down-sampled by a factor of two. Geometries were extracted from the pixelated binary images and numerical models of the metamaterials were built in COMSOL Multiphysics. Each pixel corresponds to a square mesh with four finite element nodes. In numerical calculations, each metamaterial model contained  $\approx 10^5$  square meshes to capture the deformation of unit cells by the active cell contraction. The equation for static linear elasticity is solved for the metamaterial model

$$\frac{E_{\text{bulk}}}{2(1+\nu_{\text{bulk}})(1-2\nu_{\text{bulk}})} \nabla(\nabla \cdot \mathbf{u}(\mathbf{r})) + \frac{E_{\text{bulk}}}{2(1+\nu_{\text{bulk}})} \nabla^2 \mathbf{u}(\mathbf{r}) = 0 \quad (1)$$

$\mathbf{u}(\mathbf{r})$  is the displacement vector, and  $E_{\text{bulk}}$  and  $\nu_{\text{bulk}}$  are the bulk Young’s modulus and the bulk Poisson’s ratio of IP-PDMS,  $E_{\text{bulk}} = 700$  kPa and  $\nu_{\text{bulk}} = 0.49$ , respectively. Using the plain strain module, the force at pixel was deduced as the sum of forces at four nodes. The calculated forces were scaled to match the finite thickness of the metamaterial samples.

**Analysis of Sub-Cellular Response:** The nematic order parameter of the actin cytoskeleton was determined according to previous accounts:<sup>[17]</sup>

$$\langle S \rangle = \frac{\sum_i A_i \cdot \cos(2\theta_i)}{\sum_i A_i} \quad (2)$$

$A_i$  is the area of a single actin and  $\theta_i$  is defined as the azimuth angle between the actin filament and the major axis of the cell. To quantify the density of focal adhesions (FAs), the fluorescence signals of activated vinculin was binarized using the Max-Entropy method in Fiji software, and all connected areas with

the size of 1–20 μm<sup>2</sup> were classified as FAs. The nuclear localization of YAP/TAZ was quantified following previous literature.<sup>[18]</sup> From the YAP/TAZ signals inside and outside the cell nuclei, the nuclear-to-cytoplasmic ratio ( $Nuc/Cyto$ ) of YAP/TAZ was calculated:

$$Nuc/Cyto = \frac{I_{\text{nuc}}/A_{\text{nuc}}}{I_{\text{cyto}}/A_{\text{cyto}}} \quad (3)$$

$I_{\text{nuc}}$  and  $I_{\text{cyto}}$  are the signal intensities, and  $A_{\text{nuc}}$  and  $A_{\text{cyto}}$  are the sampling areas inside and outside the cell nuclei, respectively.

**Statistical Analysis:** Statistical analysis was performed using Origin Pro 2019 (Origin Lab, Northampton, MA, USA). All box plots presented in this study present the median value as a solid line and the average value as a square. The boxes correspond to the 25–75 percentile ranges, and the whiskers to the 5–95 percentiles. Comparisons between two groups were performed using student t test. The  $p$  values < 0.05 were considered as significant difference.

## Supporting Information

Supporting Information is available from the Wiley Online Library or from the author.

## Acknowledgements

N.M. and M.F. contributed equally to this work. The authors thank the Deutsche Forschungsgemeinschaft (DFG, German Research Foundation) under Germany’s Excellence Strategy via the Excellence Cluster “3D Matter Made to Order”, EXC-2082/1-390761711 (M.T., M.B., and M.W.) and the Collaborative Research Center CRC873 (A.D.H. and M.T.), the Carl Zeiss Foundation through the “Carl-Zeiss-Foundation-Focus@HEiKA” (M.W.), the State of Baden-Württemberg (M.W.), the Helmholtz program “Materials Systems Engineering” (M.W.), and JSPS JP19H05719 (M.T.) for financial support. N.M. thanks F. J. Becker for the experimental assistance. M.T. thanks Nakatani Foundation for its support.

Open access funding enabled and organized by Projekt DEAL.

## Conflict of Interest

The authors declare no conflict of interest.

## Data Availability Statement

The data that support the findings of this study are available from the corresponding author upon reasonable request.

## Keywords

3D printing, mechanical metamaterials, mechanobiology, photoresists, stem cells

Received: January 31, 2023

Revised: March 30, 2023

Published online:

- [1] a) J. U. Surjadi, L. Gao, H. Du, X. Li, X. Xiong, N. X. Fang, Y. Lu, *Adv. Eng. Mater.* **2019**, *21*, 1800864; b) S. Bonfanti, R. Guerra, F. Font-Clos, D. Rayneau-Kirkhope, S. Zapperi, *Nat. Commun.* **2020**, *11*, 4162; c) T. Frenzel, V. Hahn, P. Ziemke, J. L. G. Schneider, Y. Chen, P. Kiefer, P. Gumbsch, M. Wegener, *Commun. Mater.* **2021**, *2*, 4; d) X. Fang, J. Wen, L. Cheng, D. Yu, H. Zhang, P. Gumbsch, *Nat. Mater.* **2022**, *21*, 869.
- [2] a) C. M. Soukoulis, S. Linden, M. Wegener, *Science* **2007**, *315*, 47; b) W. Cai, V. M. Shalae, *Optical metamaterials*, Springer, New York **2010**.
- [3] a) R. Schittny, M. Kadic, S. Guenneau, M. Wegener, *Phys. Rev. Lett.* **2013**, *110*, 195901; b) J. Wang, G. Dai, J. Huang, *iScience* **2020**, *23*, 101637.
- [4] M. Kadic, G. W. Milton, M. van Hecke, M. Wegener, *Nat. Rev. Phys.* **2019**, *1*, 198.
- [5] C. Bonnans, J. Chou, Z. Werb, *Nat. Rev. Mol. Cell Biol.* **2014**, *15*, 786.
- [6] a) A. J. Engler, S. Sen, H. L. Sweeney, D. E. Discher, *Cell* **2006**, *126*, 677; b) S. Rammensee, M. S. Kang, K. Georgiou, S. Kumar, D. V. Schaffer, *Stem Cells* **2016**, *35*, 497; c) J. M. Muncie, V. M. Weaver, in *Current Topics in Developmental Biology*, Vol. 130 (Eds: E. S. Litscher, P. M. Wassarman), Academic Press, Cambridge, MA **2018**, p. 1.
- [7] a) L. B. Case, C. M. Waterman, *Nat. Cell Biol.* **2015**, *17*, 955; b) K. Jansen, P. Atherton, C. Ballestrem, *Seminars in Cell & Developmental Biology*, Elsevier, Amsterdam **2017**.
- [8] a) W. Zhang, P. Soman, K. Meggs, X. Qu, S. Chen, *Adv. Funct. Mater.* **2013**, *23*, 3226; b) A. Maggi, H. Li, J. R. Greer, *Acta Biomater.* **2017**, *63*, 294; c) X. Chen, C. Liu, M. Wadsworth, E. Z. Zeng, T. Driscoll, C. Zeng, Y. Li, *Adv. Healthcare Mater.* **2023**, *12*, 2202511; d) G. Flamourakis, I. Spanos, Z. Vangelatos, P. Manganas, L. Papadimitriou, C. Grigoropoulos, A. Ranella, M. Farsari, *Macromol. Mater. Eng.* **2020**, *305*, 2000238; e) D. Sun, W. Liu, A. Tang, F. Zhou, *J. Biomed. Mater. Res., Part A* **2023**, *111*, 502.
- [9] V. Frank, S. Kaufmann, R. Wright, P. Horn, H. Y. Yoshikawa, P. Wuchter, J. Madsen, A. L. Lewis, S. P. Armes, A. D. Ho, M. Tanaka, *Sci. Rep.* **2016**, *6*, 24264.
- [10] M. Hippler, K. Weissenbruch, K. Richler, E. D. Lemma, M. Nakahata, B. Richter, C. Barner-Kowollik, Y. Takashima, A. Harada, E. Blasco, M. Wegener, M. Tanaka, M. Bastmeyer, *Sci. Adv.* **2020**, *6*, eabc2648.
- [11] S. Dupont, L. Morsut, M. Aragona, E. Enzo, S. Giullitti, M. Cordenonsi, F. Zanconato, J. L. e Digabel, M. Forcato, S. Bicciato, N. Elvassore, S. Piccolo, *Nature* **2011**, *474*, 179.
- [12] A. Elosegui-Artola, R. Oriá, Y. Chen, A. Kosmalska, C. Pérez-González, N. Castro, C. Zhu, X. Trepát, P. Roca-Cusachs, *Nat. Cell Biol.* **2016**, *18*, 540.
- [13] W. Wagner, R. E. Feldmann Jr, A. Seckinger, M. H. Maurer, F. Wein, J. Blake, U. Krause, A. Kalenka, H. F. Bürgers, R. Saffrich, *Exp. Hematol.* **2006**, *34*, 536.
- [14] *Cold Spring Harb. Protoc.* **2016**, 2016, <https://doi.org/10.1101/pdb.rec084301>.
- [15] J. Schindelin, I. Arganda-Carreras, E. Frise, V. Kaynig, M. Longair, T. Pietzsch, S. Preibisch, C. Rueden, S. Saalfeld, B. Schmid, *Nat. Methods* **2012**, *9*, 676.
- [16] D. G. Lowe, *Int. J. Comput. Vis.* **2004**, *60*, 91.
- [17] a) A. Zemel, F. Rehfeldt, A. E. X. Brown, D. E. Discher, S. A. Safran, *Nat. Phys.* **2010**, *6*, 468; b) H. Y. Yoshikawa, T. Kawano, T. Matsuda, S. Kidoaki, M. Tanaka, *J. Phys. Chem. B* **2013**, *117*, 4081; c) P. Linke, R. Suzuki, A. Yamamoto, M. Nakahata, M. Kengaku, T. Fujiwara, T. Ohzono, M. Tanaka, *Langmuir* **2019**, *35*, 7538.
- [18] M. Kuroda, H. Wada, Y. Kimura, K. Ueda, N. Kioka, *J. Cell Sci.* **2017**, *130*, 989.